medRxiv preprint doi: https://doi.org/10.1101/2022.08.17.22278910; this version posted August 18, 2022. The copyright holder for this preprint (which was not certified by peer review) is the author/funder, who has granted medRxiv a license to display the preprint in perpetuity. It is made available under a CC-BY-NC-ND 4.0 International license .

Non-invasive tumor probability maps developed using autopsy tissue identify novel areas of tumor beyond the imaging-defined margin

Samuel A. Bobholz[a], Allison K. Lowman[b], Jennifer M. Connelly[c], Savannah R. Duenweg[a], Aleksandra Winiarz[a], Michael Brehler[b], Fitzgerald Kyereme[b], Elizabeth J. Cochran[d], Dylan Coss[d], Benjamin M. Ellingson[e], Wade M. Mueller[f], Mohit Agarwal[b], Anjishnu Banerjee[g], Peter S. LaViolette[b,c]

[a]*Department of Biophysics, Medical College of Wisconsin*
[b]*Department of Radiology, Medical College of Wisconsin*
[c]*Department of Neurology, Medical College of Wisconsin*
[d]*Department of Pathology, Medical College of Wisconsin*
[e]*UCLA Brain Tumor Imaging Laboratory, Department of Radiological Sciences, David Geffen School of Medicine, University of California Los Angeles*
[f]*Department of Neurosurgery, Medical College of Wisconsin*
[g]*Department of Biostatistics, Medical College of Wisconsin*
[h]*Department of Biomedical Engineering, Medical College of Wisconsin*

Abstract

Background: This study identified a clinically significant subset of glioma patients with tumor outside of contrast-enhancement present at autopsy, and subsequently developed a method for detecting non-enhancing tumor using radio-pathomic mapping. We tested the hypothesis that autopsy-based radio-pathomic tumor probability maps would be able to non-invasively identify areas of infiltrative tumor beyond traditional imaging signatures. **Methods:** A total of 159 tissue samples from 65 subjects were aligned to MRI acquired nearest to death for this study. Demographic and survival characteristics for patients with and without tumor beyond the contrast-enhancing margin were computed. An ensemble algorithm was used to predict pixelwise tumor presence from pathological annotations using segmented cellularity (Cell), extracellular fluid (ECF), and cytoplasm (Cyt) density as input (6 train/3 test subjects). A second level of ensemble algorithms were used to predict voxel-wise Cell, ECF, and Cyt on the full dataset (43 train/22 test subjects) using 5-by-5 voxel tiles from T1, T1+C, FLAIR, and ADC as input. The models were then combined to generate non-invasive whole brain maps of tumor probability. **Results**: Tumor outside of contrast was identified in 41.5 percent of patients, who showed worse survival outcomes (HR=3.90, $p<0.001$). Tumor probability maps reliably tracked non-enhancing tumor in the test set, external data collected pre-surgery, and longitudinal data to identify treatment-related changes and anticipate recurrence. **Conclusions:** This study developed a multi-stage model for mapping gliomas using autopsy tissue samples as ground truth, which was able to identify regions of tumor beyond traditional imaging signatures.

Keywords: Brain cancer, MRI, machine learning, radiology, pathology

NOTE: This preprint reports new research that has not been certified by peer review and should not be used to guide clinical practice.

medRxiv preprint doi: https://doi.org/10.1101/2022.08.17.22278910; this version posted August 18, 2022. The copyright holder for this preprint (which was not certified by peer review) is the author/funder, who has granted medRxiv a license to display the preprint in perpetuity. It is made available under a CC-BY-NC-ND 4.0 International license .

1. Introduction

Glial brain tumors are the most common form of central nervous system originating tumors, with a yearly incidence of around 6 per 100,000 persons[1]. High-grade gliomas such as glioblastomas (GBMs) are often difficult to treat due to their aggressiveness and pathological heterogeneity, contributing to one- and five-year survival rates of 41 percent and 5 percent, respectively[2,3]. Current standard of care requires precise tumor localization to maximize the efficacy of frontline treatments such as surgical resection and targeted radiation therapy. Studies examining extent of resection in glioma patients have demonstrated maximizing tumor removal improves patient survival outcomes, underscoring the importance of identifying the full extent of gliomas[4–7].

Magnetic resonance imaging (MRI) is currently the primary method for non-invasive disease monitoring of gliomas. Gadolinium contrast agents are used to highlight disruptions in the blood brain barrier due to tumor angiogenesis, which results in an enhanced signal in T1-weighted imaging that is used to define the primary tumor mass[8–10]. Hyperintensities on T2-weighted fluid attenuated inversion recovery (FLAIR) images correspond to a mixture of infiltrative tumor and edema, though differentiating between tumor and non-tumor remains a source of uncertainty in imaging interpretation[11–14]. Apparent diffusion coefficient (ADC) images derived from diffusion-weighted imaging have shown promise in highlighting areas of diffusion restricting hypercellularity associated with tumor, though recent studies validating this signature beyond the contrast-enhancing margin have disputed the strength of this relationship[14–19]. Machine learning approaches have also sought to maximize the amount of clinically relevant information we can extract from these non-invasive images, employing recent advances in computing to automatically segment the radiologist-defined margin, identify patient-level genetic signatures such as IDH1 mutation and MGMT methylation status, and predict cellular-level information using biopsy samples as validation[20–24].

Despite the promise of these recent techniques, identifying areas of tumor beyond the contrast- and FLAIR-enhancing margins remain particularly difficult. Studies of autopsy tissue samples aligned to MRI acquired near death have found areas of active tumor as far as 10 cm beyond the treated margin, indicating the need for improvements in tumor tracking[17,25,26]. However, identifying regions of tumor beyond current signatures requires ground truth tissue samples from beyond the suspected tumor region, which is beyond the capabilities of studies using biopsy tissue and radiologist annotations as the gold standard. Therefore, studies with access to tissue beyond contrast enhancement are essential for identifying the true extent of tumor, particularly in the less-studied post-treatment state. This study uses autopsy tissue samples, collected both within and beyond the traditional tumor margin, to assess the prevalence of tumor outside the MRI-defined margin and develop a multi-stage model for non-invasive tumor probability mapping. Specifically, we tested the hypothesis that an MRI-based model for tumor probability trained on autopsy tissue samples can track glioma invasion beyond the currently defined margin.

2. Methods

2.1. Patient Population

This study was approved by the Institutional Review Board of Medical College of Wisconsin. Written, informed consent was obtained from 65 patients to participate in this study,

medRxiv preprint doi: https://doi.org/10.1101/2022.08.17.22278910; this version posted August 18, 2022. The copyright holder for this preprint (which was not certified by peer review) is the author/funder, who has granted medRxiv a license to display the preprint in perpetuity. It is made available under a CC-BY-NC-ND 4.0 International license .

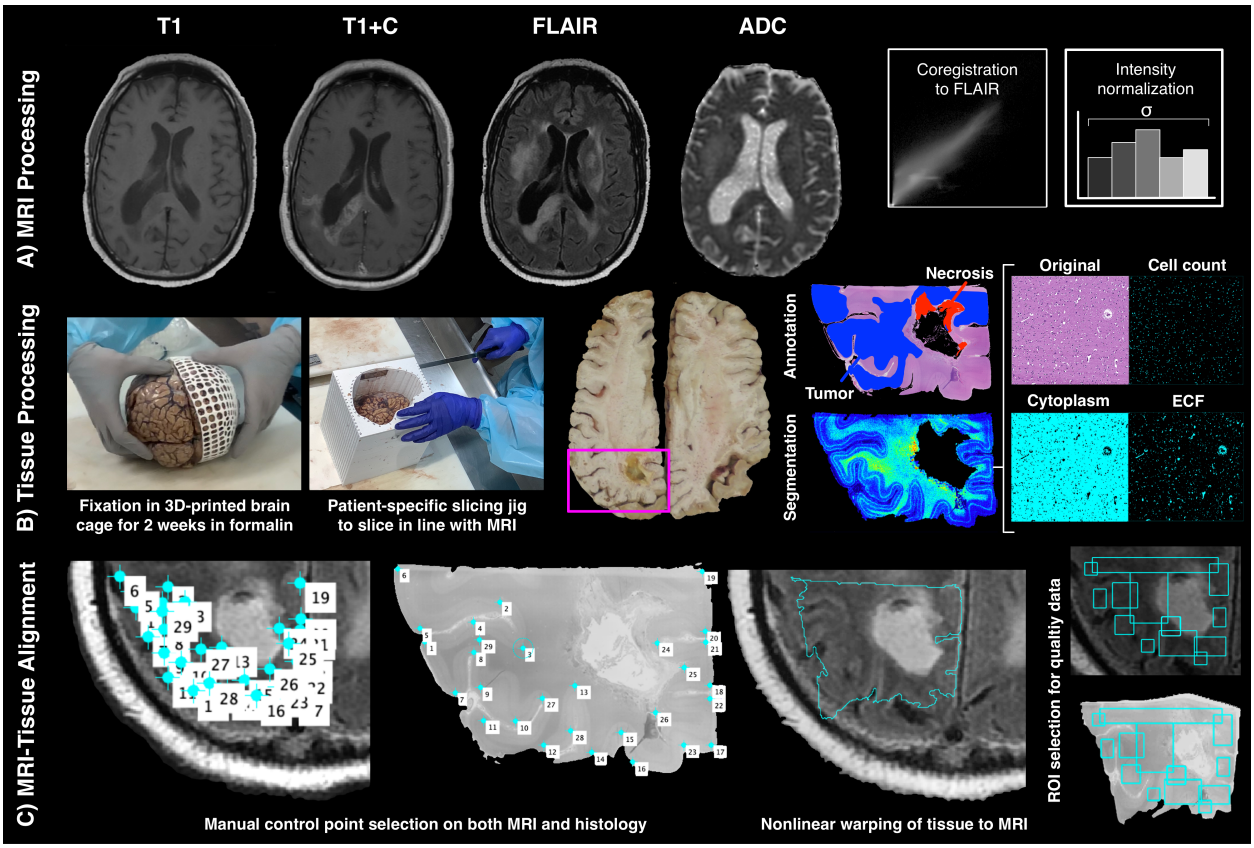

Figure 1: Overview of data collection process. A) T1, T1+C, FLAIR, and ADC scans are collected from each patient's last imaging session prior to death. All scans are aligned to the FLAIR image and qualitative scans are intensity normalized by the within-brain standard deviation. B) Brains are formalin-fixed in 3D printed brain cages to prevent distortion, and patient specific slicing jigs are used to slice brains in alignment with each patient's MRI. Tissue is then digitized and segmented into different tissue features, and a subset of patients is annotated for tumor presence. C) Tissue data is then warped to the MRI using manually defined control points, and regions of interest are drawn to selectively include areas of high-quality tissue and MRI data.

each diagnosed with a glioma in concordance with the 2021 WHO classification standards for brain tumors. These participants were divided into a training dataset used for model development and a test set used to test model generalizability. Clinical and demographic characteristics of this sample, as well as for the subsamples relevant to this study, are presented in **Supplemental Table 1**. A schematic of the overall study outline and data processing steps is presented in **Figure 1**.

2.2. MR Image Acquisition and Preprocessing

Clinical imaging from each patient's last MRI session prior to death was collected for use in this study. Due to the use of clinical imaging, acquisition parameters were not standardized across patients. T1, T1+C, FLAIR, and ADC images were selected as the primary focus for this study, as they provide a wide range of information regarding tissue characteristics while remaining ubiquitous across clinical acquisitions. T1, T1+C, and ADC images were each rigidly aligned to the FLAIR image using SPM12 (https://www.fil.ion.ucl.ac.uk/spm). Qualitative images (T1, T1+C, and FLAIR) were then divided by the intensity standard deviation within the brain to normalize values across patients[8,14]. For the test set, MRI

medRxiv preprint doi: https://doi.org/10.1101/2022.08.17.22278910; this version posted August 18, 2022. The copyright holder for this preprint (which was not certified by peer review) is the author/funder, who has granted medRxiv a license to display the preprint in perpetuity. It is made available under a CC-BY-NC-ND 4.0 International license .

sessions from the patient's entire clinical history were collected, aligned to the FLAIR nearest to death, and normalized to assess the ability of the model to track tumor growth patterns over time.

2.3. Tissue Segmentation and Processing

A total of 159 tissue samples were collected from participants at autopsy using previously described methods and placed in 66 mm by 49 mm large format cassettes[14,17,26]. Following hematoxylin and eosin (HE) staining, digitization at 40X magnification, and downsizing by a factor of 10, a color deconvolution algorithm was used to separate the images into color channels that correspond to stain optical density (i.e., positive hematoxylin staining, positive eosin staining, background)[27]. This image was then filtered and processed to extract nuclei, cytoplasm (Cyt,), and extracellular fluid (ECF). Both segmentations were then upsampled to approximate MRI resolution, using 50x50 superpixels to convert segmentation masks to cell density (cells/mm^2) and ECF/Cyt proportion (ranging from 0 to 1). Additionally, 33 tissue samples from a subset of 9 participants were annotated for presence of infiltrative tumor (IT), tumor with pseudopalisading necrosis (PN), non-tumor necrosis (NtN), and unlabeled tissue (UL) by a pathologist-trained technician.

2.4. MRI-Histology Co-registration

Tissue samples were aligned to each participant's FLAIR image using previously published in-house software, written in Matlab[14,17,26,28,29]. Manually defined control points were used to identify architectural landmarks on both the tissue data and the MRI using photos from autopsy to guide accurate placement. These control points were then used to compute a non-linear transform that warped tissue to the same space as the MRI, and regions of interest were drawn to exclude areas of tissue distortion (i.e., rips, tears, folds) and MRI artifacts. Following MRI-tissue co-registration, all MRI and tissue data was resampled to 0.4397 X 0.4397 mm per pixel resolution to harmonize all subjects to the most common acquisition parameters.

2.5. Assessing prevalence of tumor beyond MRI-defined margin

Aligned autopsy tissue was then compared to the T1+C MRI to estimate the prevalence of tumor outside of contrast enhancement (TOC). Tissue samples were visually inspected for tumor presence using histological characteristics (i.e. hypercellularity, mitotic events, pseudopalisading necrosis), as well as any annotations or immunohistochemical staining available (i.e., Ki-67, CD31). Patients were then coded for presence of TOC by comparing manually segmented maps of contrast to the aligned tissue samples (see **Supplemental Figure 1** for examples). Chi-squared tests were also used to determine differences in TOC frequency amongst patients who did and did not receive radiation with temozolomide (Rad+TMZ), Bevacizumab (Bev), and tumor treating fields (TTFields), as well as amongst diagnostic grade groups. A Cox proportional hazards regression was then fit to compare survival durations between patients with and without TOC, including time between MRI and death as a covariate. Survival curves were limited to patients who had received standard treatment (Rad+TMZ) to exclude a small number of untreated patients who tended to survive shorter than similar patients who had received treatment. Analysis was performed for the full data set (N=65), as well as on subjects with scans less than 90 days away from death (N=47) and

medRxiv preprint doi: https://doi.org/10.1101/2022.08.17.22278910; this version posted August 18, 2022. The copyright holder for this preprint (which was not certified by peer review) is the author/funder, who has granted medRxiv a license to display the preprint in perpetuity. It is made available under a CC-BY-NC-ND 4.0 International license .

patients with a primary GBM at first surgery (N=37) to compare results across potential confounds.

2.6. Predicting tumor presence from pathological segmentations

A chart indicating the flow of patients across the multiple model training stages is presented in **Supplemental Figure 2**. The first component of the multi-stage tumor prediction model involved predicting tumor annotations from the segmented pathology data. Several different candidate models were assessed, including k-nearest neighbors, naïve bayes, decision trees, and random-under-sampling-boosted random forest (RUS Tree) models. Each model was trained using pixelwise cell, Cyt, and ECF density as input to predict tumor annotation (IT and PN) versus non-tumor (NtN and UL). Models were trained on slides from 6 subjects and validated on the 3 remaining subjects to assess generalizability. Model performance was evaluated using receiver operator characteristic (ROC) plots and area under the curve (AUC) metrics. The model with the highest AUC was then incorporated into the multi-stage model.

2.7. Predicting pathological segmentations from MRI data

The second stage of the multi-stage model focused on training separate models to predict cell, Cyt, and ECF density using MRI data. Bootstrap aggregating (bagging) random forest models were trained to predict voxel-wise densities using 5 by 5 voxel tiles from the T1, T1+C, FLAIR and ADC as input. This model framework was selected based on our previous publication, which developed a proof-of-concept model for predicting cellularity using MRI data in a smaller sample of patients[25]. These models were developed on 2/3rds of the full dataset (N=43) and tested on the held-out test set (n=22) to assess generalizability. None of the patients in the pathological tumor prediction test set overlapped with the training set for these radio-pathomic models, ensuring that the test set contained only data unseen in training for every component model. Quantitative performance was evaluated using root-mean-squared error (RMSE) estimates within each test set subject, and example segmentations were plotted and compared to ground truth segmentations to ensure accurate spatial localization of cell, ECF, and Cyt trends. Predicted maps for cellularity were set to range from 0 to 6000+ cells/mm^2, which offered good contrast between hypercellular tumor and normal tissue when examining tissue samples, and ECF/Cyt density maps were set to range from 0 to 1, reflecting the minimum and maximum possible values of the measurement.

2.8. Predicting tumor presence from MRI data

Following model training, the best performing pathological tumor prediction model was used to convert whole brain cell, ECF, and Cyt density maps to tumor probability maps (TPMs). These maps were then plotted against predicted segmentations to assess patterns in what the model classifies as tumor, as well as against ground truth tissue segmentations and annotations to assess accuracy at identifying novel tumor beyond traditional signatures. TPMs were then applied to longitudinal images from all applicable timepoints across each test set patient's clinical history to assess the ability for our tumor prediction model to identify areas of pre-angiogenic recurrent tumor prior to contrast enhancement. Additionally, whole brain TPMs were applied to two external data sets to assess the quality of the maps (i.e., free from artifacts, noise) and ability to identify non-enhancing tumor on MRI data

medRxiv preprint doi: https://doi.org/10.1101/2022.08.17.22278910; this version posted August 18, 2022. The copyright holder for this preprint (which was not certified by peer review) is the author/funder, who has granted medRxiv a license to display the preprint in perpetuity. It is made available under a CC-BY-NC-ND 4.0 International license .

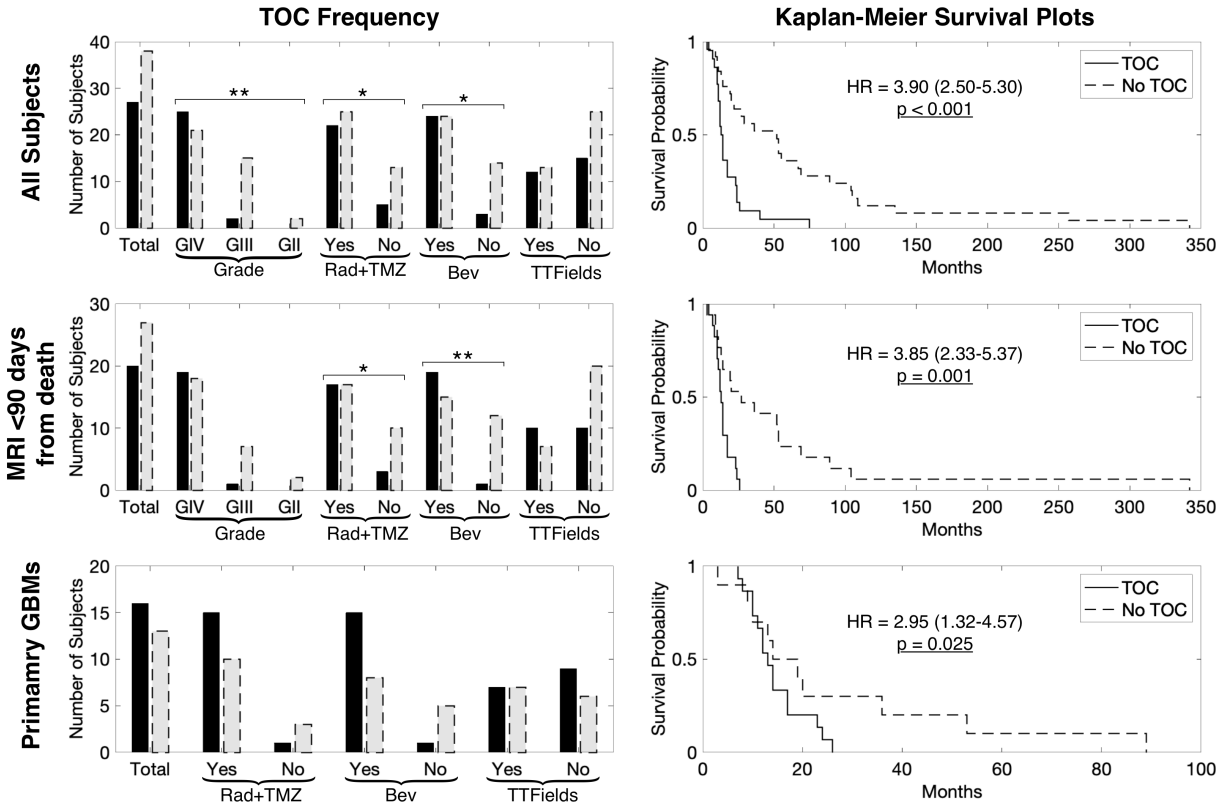

Figure 2: Prevalence and survival analyses for patients with tumor outside contrast enhancement. Analyses were performed separately for the full dataset, patients with MRI less than 90 days prior to death, and patients with a primary GBM. Survival analyses were conducted using Cox proportional hazards regression and only include patients who have received Rad+TMZ treatment. Results indicate increased TOC frequency amongst GBMs and patients who have received Rad+TMZ or Bev treatment. Patients with TOC also show reduced survival compared to patients without TOC. *p<0.05, **p<0.01

acquired entirely independently of this study. The first external subject was a 61 year old male diagnosed with a recurrent GBM, whose scan was collected by our external collaborators at the University of California – Los Angeles. The second external case was a pre-treatment acquisition from a 50 year old male diagnosed with GBM, taken from the publicly available TCGA-GBM dataset (https://cancergenome.nih.gov/)[30,31].

3. Results

3.1. Prevalence of non enhancing tumor

Figure 2 shows the prevalence estimates for TOC presence, as well as corresponding Kaplan-Meier plots for survival analyses. TOC was observed in 41.5 percent of patients, with increased presence amongst GBM (GIV) patients (χ^2=10.73, p=0.005), patients who have been treated with Rad+TMZ (χ^2=3.99, p=0.046), and patients treated with bevacizumab (Bev) (χ^2=5.41, p=0.020). Treated patients with TOC showed decreased survival rates compared to patients without TOC (HR=3.90, 95 percent CI = 2.50-5.30, p<0.001). Patients with MRI data from within 90 days of death also showed increased TOC presence amongst Rad-TMZ and bevacizumab-treated (χ^2=4.50, p=0.033 and χ^2=4.50, p=0.033, respectively)

medRxiv preprint doi: https://doi.org/10.1101/2022.08.17.22278910; this version posted August 18, 2022. The copyright holder for this preprint (which was not certified by peer review) is the author/funder, who has granted medRxiv a license to display the preprint in perpetuity. It is made available under a CC-BY-NC-ND 4.0 International license .

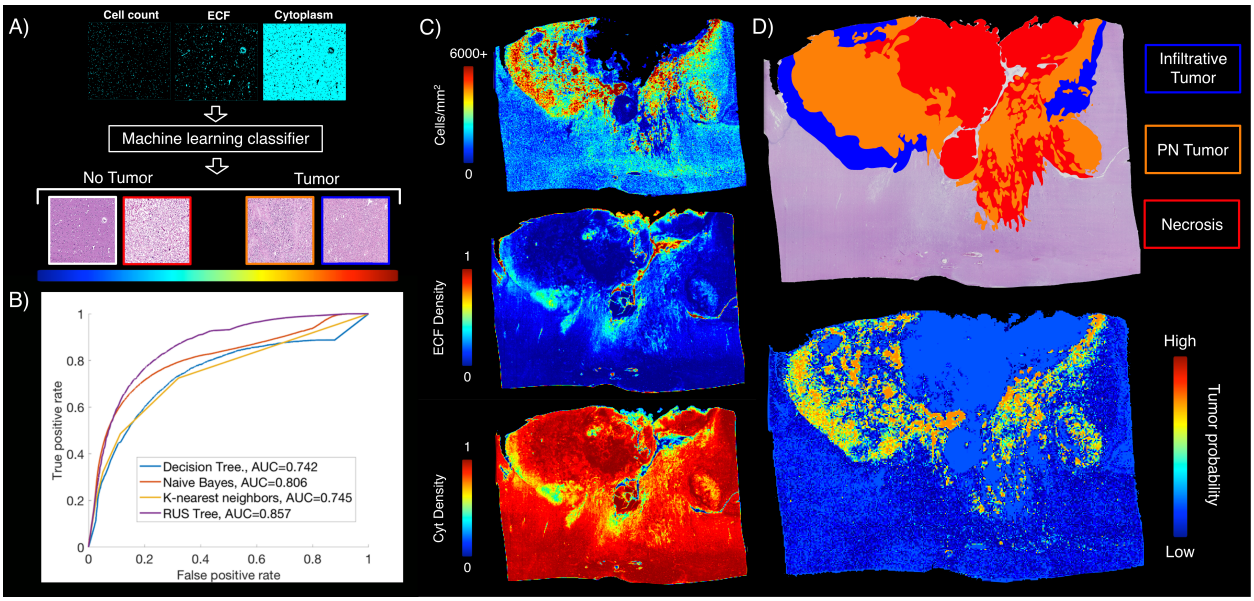

Figure 3: Pathological tumor prediction. A) The pathological tumor prediction model uses cell density, ECF, and Cyt segmentations to distinguish tumor vs. non-tumor using the pathological annotations as ground truth. B) The RUS Tree algorithm was the highest performing tumor prediction model (AUC=0.857) and was used in the final multi-stage TPM model. C) Example tumor probability maps from the RUS Tree model show accurate tumor prediction in both IT and PN areas, while avoiding both normal tissue and areas of necrosis.

patients, and reduced survival associated with TOC (HR = 3.85, 95 percent CI = 2.33-5.37, p = 0.001). Primary GBM patients did not show significant differences in TOC presence with respect to treatment but did show reduced survival within patients with TOC (HR = 2.95, 95 percent CI = 1.32-4.57, p = 0.025).

3.2. Predicting tumor presence from pathological segmentations

Figure 3 shows the performance results for the pathological tumor prediction model, along with example tumor probability maps and corresponding ground truth annotations. The RUS Tree model gave the best ROC AUC of 0.857 and was therefore selected as the model used to convert MRI-based pathological segmentations into tumor probability maps. Example predictions show good concordance between areas of high tumor probability and actual tumor presence within both IT and PN tumor types, while correctly avoiding edema and other non-tumor areas.

3.3. Predicting pathological segmentations from MRI data

Segmentation prediction results are shown in **Figure 4**, along with example whole brain predictions on test set subjects. Each radio-pathomic model had a mean subject-level RMSE value within a standard deviation of the ground truth (cell density Std. RMSE = 0.756, Cyt Std. RMSE = 0.917, ECF Std. RMSE = 0.941), indicating satisfactory model performance for each tissue type. Example predictions indicate regions where these maps improve pathological interpretations of the MRI data, such as discrimination between areas of edema and hypercellularity within the FLAIR hyperintense region and areas of hypercellularity beyond contrast enhancement.

medRxiv preprint doi: https://doi.org/10.1101/2022.08.17.22278910; this version posted August 18, 2022. The copyright holder for this preprint (which was not certified by peer review) is the author/funder, who has granted medRxiv a license to display the preprint in perpetuity. It is made available under a CC-BY-NC-ND 4.0 International license .

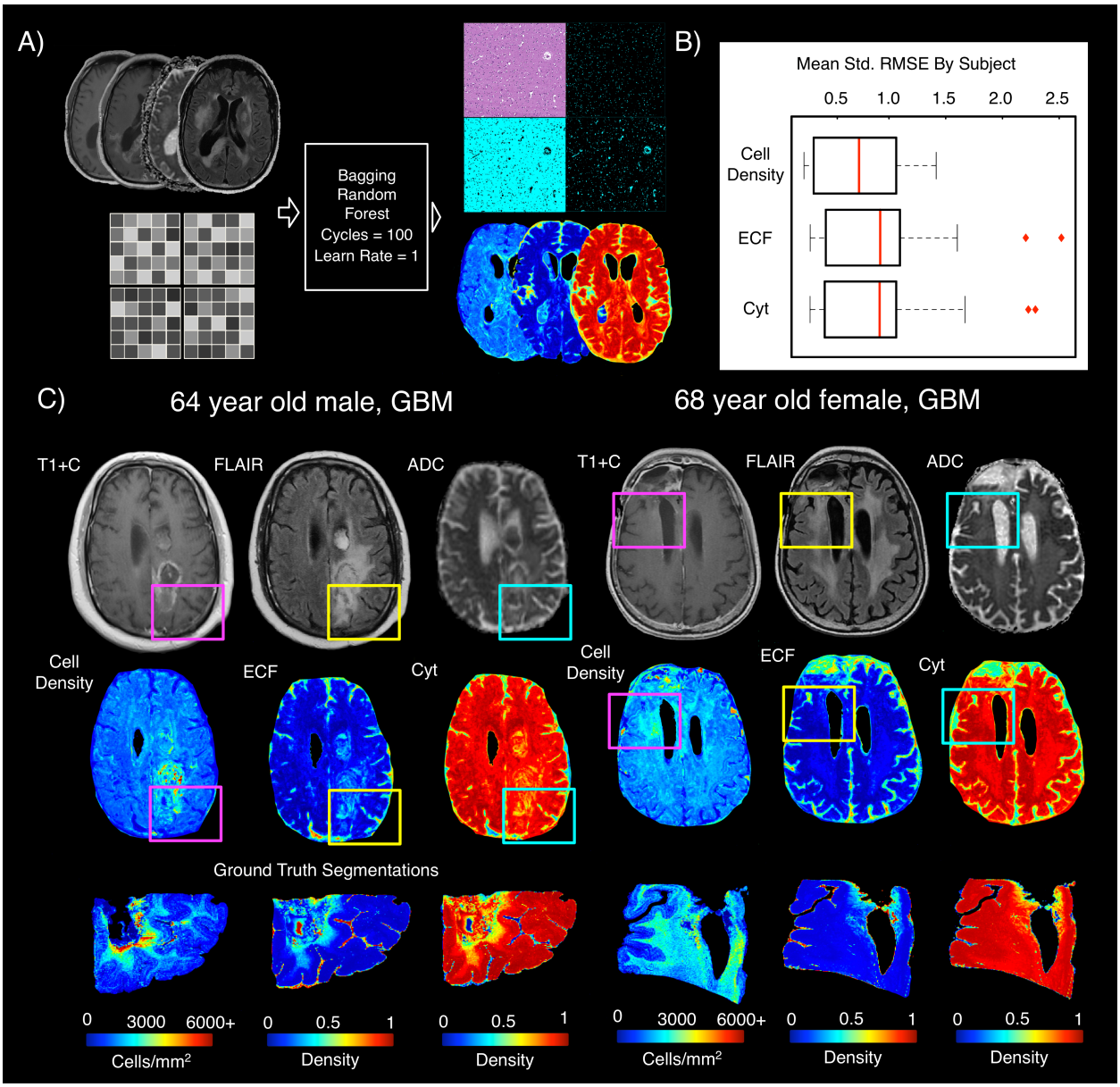

Figure 4: Radio-pathomic maps of tissue segmentations. A) 5 by 5 voxel tiles from T1, T1+C, FLAIR, and ADC were used to predict voxelwise cell density, ECF, and Cyt using bagging random forests. B) Test set performance indicates an average subject-level RMSE within a standard deviation of the tissue ground truth for each tissue class, indicating satisfactory model performance for most subjects. C) Example tissue predictions show areas of accurately predicted cellularity beyond contrast enhancement, as well as distinguishing between vasogenic edema and hypercellular areas within the FLAIR hyperintense region. The subject on the left shows a portion of hypercellularity extending posterior to the contrast-enhancing margin, while highlighting a reduction in cell density within the FLAIR hyperintensity anterior to the contrast-enhancement. The subject on the right shows an area of increased cellularity in the absence of contrast enhancement and diffusion restriction.

3.4. Predicting tumor presence from MRI data

An example TPM generated from the full multi-stage model are presented in **Figure 5**. Test set TPM with pathological annotations available showed good correspondence between

medRxiv preprint doi: https://doi.org/10.1101/2022.08.17.22278910; this version posted August 18, 2022. The copyright holder for this preprint (which was not certified by peer review) is the author/funder, who has granted medRxiv a license to display the preprint in perpetuity. It is made available under a CC-BY-NC-ND 4.0 International license .

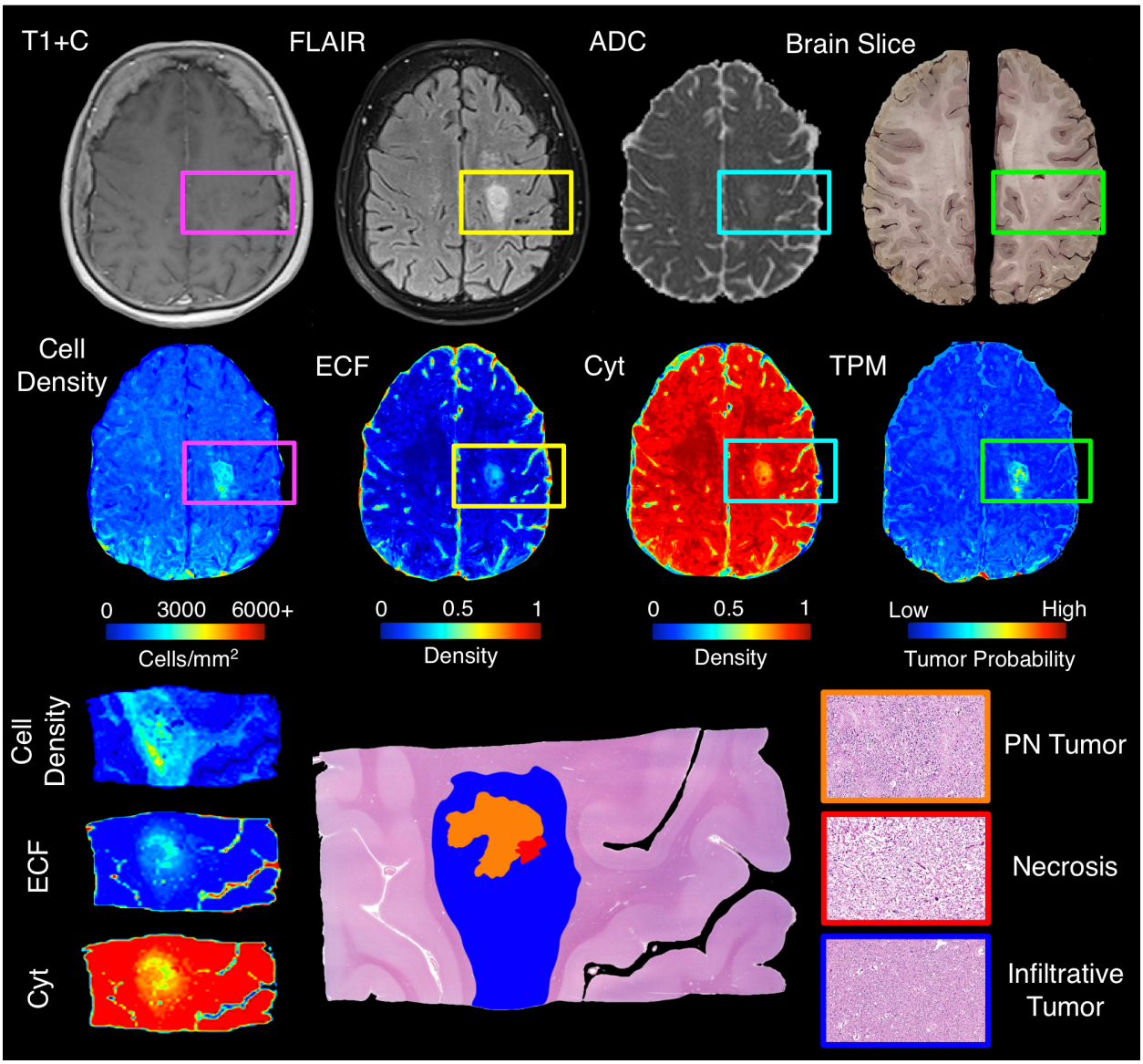

Figure 5: Example TPM for a test set subject (GBM, Female, 80yo) , along with corresponding MRI and segmentation predictions. The TPM for this patient accurately highlights an area of tumor outside contrast enhancement and in the absence of diffusion restriction. In addition, the cell density map highlights that the entire tumor area is hypercellular, while the ECF map highlights a high-ECF core to the hypercellular area, which correctly suggests an area of pseudopalisading necrosis (high cellularity, high ECF). This demonstrates the ability for TPMs to distinguish between pathologically distinct regions of tumor.

areas of predicted and actual tumor, with separation between areas of PN (high cellularity, high ECF) and areas of non-PN tumor (high cellularity, normal ECF) seen on the corresponding segmentation maps. Tumor was also accurately observed beyond the contrast enhancing region. External data and longitudinal TPMs are presented in **Figure 6**. Predictions on external data sets demonstrated that TPMs generated from this framework provided low-noise, interpretable maps on new data, as well as identified new areas of possible tumor infiltration beyond contrast enhancement. Longitudinal predictions for the example subject showed

medRxiv preprint doi: https://doi.org/10.1101/2022.08.17.22278910; this version posted August 18, 2022. The copyright holder for this preprint (which was not certified by peer review) is the author/funder, who has granted medRxiv a license to display the preprint in perpetuity. It is made available under a CC-BY-NC-ND 4.0 International license .

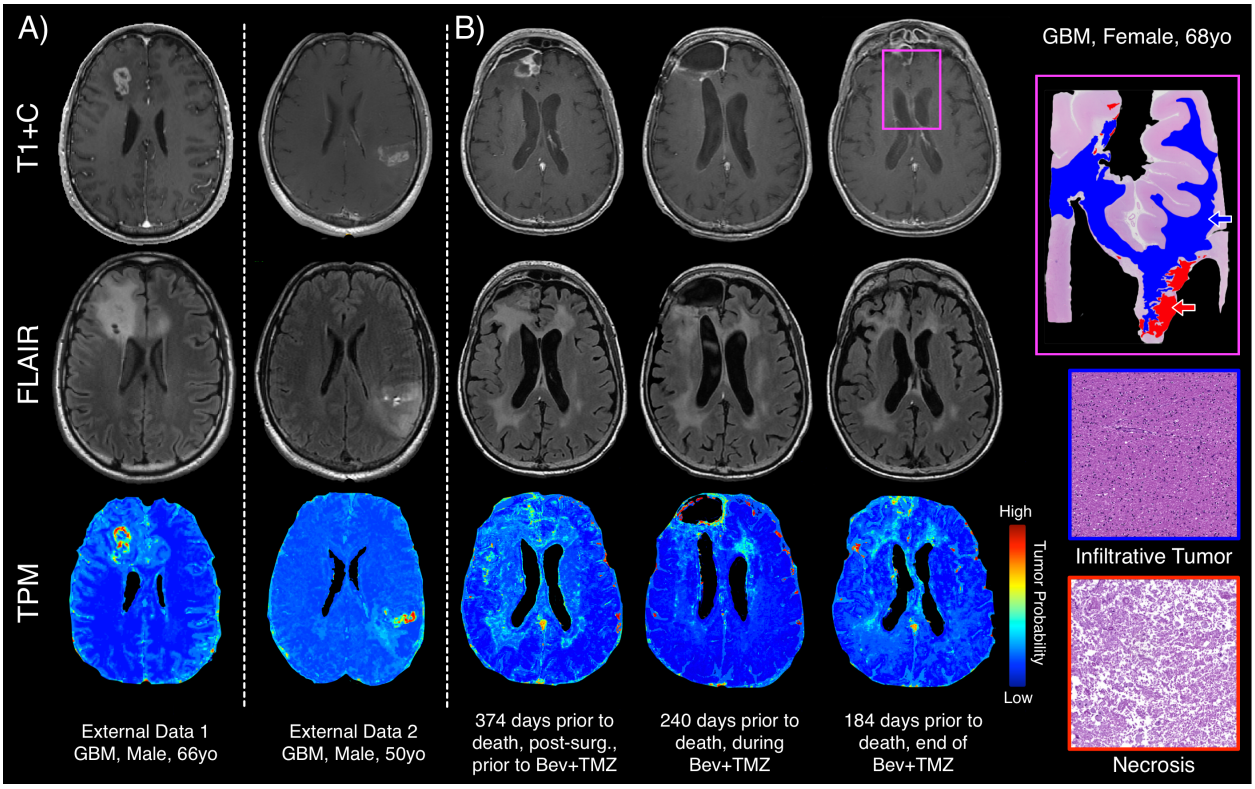

Figure 6: External and longitudinal TPMs. A) Example TPMs applied to externally collected data show similar quality TPMs to those included in our study and show areas of predicted tumor beyond contrast enhancement. B) Longitudinal TPMs show early indications of tumor crossing over into the contralateral hemisphere 374 days prior to death, with confirmed tumor in this region at autopsy. Additionally, the TPMs show a decrease in tumor probability in response to Bev+TMZ treatment that returns to pre-treatment levels after treatment cessation, suggesting TPMs may be able to visualize the effects of treatment on non-enhancing portions of tumor.

the TPM in response to treatment, where areas of heightened tumor probability tended to fade after administration of Bev+TMZ and returned following treatment cessation. These maps also identified tumor crossing-over into the contralateral hemisphere as early as 374 days prior to death despite a lack of contralateral contrast enhancement across the patient's imaging. This area of crossing over was confirmed to be tumor at autopsy.

4. Discussion

This study developed a multi-stage tumor prediction model that accurately identifies areas of infiltrative tumor beyond traditional imaging signatures. A pathological tumor prediction model based on histology segmentations was combined with MRI-based maps of tissue composition to bridge the gap between histopathological assessment and non-invasive tracking of glioma. We validated this technique using autopsy tissue samples collected near death as ground truth, and successfully applied our models to external data to demonstrate generalizability. Furthermore, we showed that these models can detect areas of tumor recurrence prior to contrast enhancement in retrospective longitudinal data from our test set patients, indicating further clinical utility in disease tracking across patients' clinical

medRxiv preprint doi: https://doi.org/10.1101/2022.08.17.22278910; this version posted August 18, 2022. The copyright holder for this preprint (which was not certified by peer review) is the author/funder, who has granted medRxiv a license to display the preprint in perpetuity. It is made available under a CC-BY-NC-ND 4.0 International license .

histories. This study is the first of its kind to provide tumor probability maps validated using tissue well-beyond the current treatment margin, and is, to date, the largest study of radio-pathomic signatures at autopsy in brain cancer.

This study demonstrates that around half of gliomas exist in part beyond the treated margin, with higher rates observed in higher grade tumors such as glioblastomas. Since this study only used select tissue samples from areas of suspected tumor that could be aligned accurately to the MRI after tissue processing, this frequency is likely a lower bound, as it is possible that areas of tumor are missed in the tissue sample selection process. However, this prevalence estimate highlights that tumor outside of contrast enhancement is present in most cases, and targeted future MRI-based research should focus on these regions specifically to improve non-invasive tumor localization. In addition, future research at the molecular level could identify pathologic or genetic signatures of enhancing versus non-enhancing tumors, because a better understanding of how tumor evades current detection mechanisms could drive future treatments directed at these non-angiogenic areas of tumor. This is particularly crucial to understanding tumor in the treated state, as our preliminary assessment of treatment effects on TOC/TOF highlight treatment's impact on radio-pathomic relationships. Bevacizumab in combination with Rad+TMZ treatment was associated with greater tumor outside of contrast compared to bevacizumab-naïve patients, which is hypothesized to be caused by the anti-angiogenic treatment disrupting the co-occurrence of tumor and contrast enhancement. In the future, more targeted research should be conducted to elucidate the mechanism of this relationship further, as well as to understand the influence of factors such as treatment duration and timing on non-enhancing tumor invasion.

To detect regions of tumor beyond traditional imaging signatures, we developed a multi-stage model to predict tumor using autopsy tissue samples as ground truth. Prior research attempting similar tasks have used biopsy tissue samples, which, while useful, inherently fail to capture areas of tumor beyond the treated margin[19,32–34]. Our prior studies of autopsy tissue samples have highlighted how imaging signatures validated within contrast enhancement, such as an inverse relationship between ADC and cellularity, tend to show much weaker relationships when validated using tissue from beyond the enhancing region[14,17]. Our prior paper also developed a proof-of-concept model for predicting cellularity using autopsy tissue samples, which, while insightful, does not directly correlate with areas of tumor, as not all tumor regions (i.e., areas of pseudopalisading necrosis) are strictly hypercellular and not all areas of increased cellularity (i.e., areas of immune response) are tumor[25]. This study sought to expand upon this method by incorporating multiple tissue segmentations to predict tumor presence itself. In addition to providing precise assessments of tumor presence to distinguish between regions of tumor and non-tumor, the tissue segmentations for cellularity, ECF, and cytoplasm aided in interpreting different features of tumor, such as distinguishing between areas of PN and non-PN tumor, as well as differentiating between areas of tumor and vasogenic edema within FLAIR hyperintensity. This highlights how providing a rich pathological ground truth can vastly improve non-invasive tumor tracking, particularly using machine learning techniques to map relationships invisible to the naked eye.

In addition to applying our model to a held-out test set to assess model performance near death, we applied our model to longitudinal imaging throughout patients' clinical history to assess our model's ability to predict recurrence prior to contrast enhancement. A subset of cases showed areas of predicted tumor that became contrast-enhancing tumor months later,

medRxiv preprint doi: https://doi.org/10.1101/2022.08.17.22278910; this version posted August 18, 2022. The copyright holder for this preprint (which was not certified by peer review) is the author/funder, who has granted medRxiv a license to display the preprint in perpetuity. It is made available under a CC-BY-NC-ND 4.0 International license .

and some subjects even showed areas of infiltrative tumor beyond contrast enhancement months prior to death that never became contrast-enhancing but did in fact contain tumor at autopsy. Though future research using biopsy samples is required to confirm tumor presence at timepoints prior to death, these results suggest that TPMs may identify tumor prior to its visual appearance on traditional imaging. By applying this technique to retrospective data and previously collected clinical trials, these maps may be able to reveal new signatures of treatment response in terms of reduced hypercellular volume and low tumor probability, which in turn could identify subsets of patients that selectively respond to treatment.

4.1. Limitations

Due to the use of autopsy tissue samples, the time between imaging and death is an important limiting factor in this study. It is likely that tumor continues to grow near death, and imaging acquired months before death may not reflect how the patient's imaging would look immediately prior to death. We have accounted for this in our study by restricting our frequency assessment of tumor outside contrast enhancement to imaging within two months of death and have matched our train and test data sets for time between MRI and death. However, future studies using longitudinal imaging to model tumor growth rates may control for this factor more precisely. Post-mortem MRI has also been considered as an alternative, however the changes in tissue properties post-fixation and inability to collect common brain cancer imaging acquisitions (i.e., T1+C) would hinder the ability for our models to predict tumor on clinical data. It is also possible that tissue distortions that have occurred during processing may result in imperfect alignment with MRI data; however, our previously published tissue processing protocol controls for this factor at every step of the tissue collection process, and regions of interest defined after non-linear warping are used to exclude regions of suboptimal tissue quality. Additionally, while this is the largest study of its kind using an unprecedented amount of autopsy tissue data aligned to MRI, the validation set for this study was relatively small compared to other machine learning studies. Our predictions on external data sets highlight the feasibility of applying this method to large data sets for further validation, but precise validation using tissue samples remains an area of future research beyond the scope of this study.

4.2. Conclusion

This study used autopsy tissue samples aligned to MRI to develop a multi-stage model for tumor probability to predict areas of non-enhancing tumor that occur in most glioma patients in our data set. This model accurately identified regions of tumor beyond traditional imaging signatures, provided information for distinguishing between hypercellular and necrotic areas of tumor, and identified distinct phenotypes based on the maps that differ in survival and treatment efficacy. This technique has the potential to improve disease tracking in the post-treated state and could expand the treated margin to encompass additional infiltrative tumor missed by current tracking techniques. This improvement in disease tracking can thus improve treatment efficacy and clinical outcomes.

5. Disclosures

Authors PSL and JMC receive funding from Novacure Inc. unrelated to the scope of this study.

medRxiv preprint doi: https://doi.org/10.1101/2022.08.17.22278910; this version posted August 18, 2022. The copyright holder for this preprint (which was not certified by peer review) is the author/funder, who has granted medRxiv a license to display the preprint in perpetuity. It is made available under a CC-BY-NC-ND 4.0 International license .

6. Data Availability

The MRI and histology data sets used in this study are not currently publicly available due to data usage agreement restrictions. De-identified data is available upon reasonable request.

References

[1] Ostrom QT, Cioffi G, Gittleman H, et al. CBTRUS Statistical Report: Primary Brain and Other Central Nervous System Tumors Diagnosed in the United States in 2012-2016. Neuro Oncol. 2019;21(Suppl 5):v1-v100. doi:10.1093/neuonc/noz150

[2] Ostrom QT, Cote DJ, Ascha M, Kruchko C, Barnholtz-Sloan JS. Adult Glioma Incidence and Survival by Race or Ethnicity in the United States From 2000 to 2014. JAMA Oncol. 2018;4(9):1254-1262. doi:10.1001/jamaoncol.2018.1789

[3] Mathew EN, Berry BC, Yang HW, Carroll RS, Johnson MD. Delivering Therapeutics to Glioblastoma: Overcoming Biological Constraints. Int J Mol Sci. 2022;23(3). doi:10.3390/ijms23031711

[4] Behling F, Rang J, Dangel E, et al. Complete and Incomplete Resection for Progressive Glioblastoma Prolongs Post-Progression Survival. Front Oncol. 2022;12:755430. doi:10.3389/fonc.2022.755430

[5] Karschnia P, Vogelbaum MA, van den Bent M, et al. Evidence-based recommendations on categories for extent of resection in diffuse glioma. Eur J Cancer. 2021;149:23-33. doi:10.1016/j.ejca.2021.03.002

[6] Aabedi AA, Young JS, Zhang Y, et al. Association of Neurological Impairment on the Relative Benefit of Maximal Extent of Resection in Chemoradiation-Treated Newly Diagnosed Isocitrate Dehydrogenase Wild-Type Glioblastoma. Neurosurgery. 2022;90(1):124-130. doi:10.1227/NEU.0000000000001753

[7] Skardelly M, Kaltenstadler M, Behling F, et al. A Continuous Correlation Between Residual Tumor Volume and Survival Recommends Maximal Safe Resection in Glioblastoma Patients: A Nomogram for Clinical Decision Making and Reference for Non-Randomized Trials. Front Oncol. 2021;11:748691. doi:10.3389/fonc.2021.748691

[8] Ellingson BM, Aftab DT, Schwab GM, et al. Volumetric response quantified using T1 subtraction predicts long-term survival benefit from cabozantinib monotherapy in recurrent glioblastoma. Neuro Oncol. 2018;20(10):1411-1418. doi:10.1093/neuonc/noy054

[9] Tixier F, Um H, Young RJ, Veeraraghavan H. Reliability of tumor segmentation in glioblastoma: impact on the robustness of MRI-radiomic features. Med Phys. 2019. doi:10.1002/mp.13624

medRxiv preprint doi: https://doi.org/10.1101/2022.08.17.22278910; this version posted August 18, 2022. The copyright holder for this preprint (which was not certified by peer review) is the author/funder, who has granted medRxiv a license to display the preprint in perpetuity. It is made available under a CC-BY-NC-ND 4.0 International license .

[10] He L, Huang Y, Ma Z, Liang C, Liang C, Liu Z. Effects of contrast-enhancement, reconstruction slice thickness and convolution kernel on the diagnostic performance of radiomics signature in solitary pulmonary nodule. Sci Rep. 2016;6:34921. doi:10.1038/srep34921

[11] Husstedt HW, Sickert M, Köstler H, Haubitz B, Becker H. Diagnostic value of the fast-FLAIR sequence in MR imaging of intracranial tumors. Eur Radiol. 2000;10(5):745-752. doi:10.1007/s003300050997

[12] Garrett MD, Yanagihara TK, Yeh R, et al. Monitoring Radiation Treatment Effects in Glioblastoma: FLAIR Volume as Significant Predictor of Survival. Tomogr (Ann Arbor, Mich). 2017;3(3):131-137. doi:10.18383/j.tom.2017.00009

[13] Hawkins-Daarud A, Rockne RC, Anderson ARA, Swanson KR. Modeling Tumor-Associated Edema in Gliomas during Anti-Angiogenic Therapy and Its Impact on Imageable Tumor. Front Oncol. 2013;3:66. doi:10.3389/fonc.2013.00066

[14] Bobholz SA, Lowman AK, Barrington A, et al. Radiomic Features of Multiparametric MRI Present Stable Associations With Analogous Histological Features in Patients With Brain Cancer. Tomogr (Ann Arbor, Mich). 2020;6(2):160-169. doi:10.18383/j.tom.2019.00029

[15] Eidel O, Neumann J-O, Burth S, et al. Automatic Analysis of Cellularity in Glioblastoma and Correlation with ADC Using Trajectory Analysis and Automatic Nuclei Counting. PLoS One. 2016;11(7):e0160250. doi:10.1371/journal.pone.0160250

[16] LaViolette PS, Mickevicius NJ, Cochran EJ, et al. Precise ex vivo histological validation of heightened cellularity and diffusion-restricted necrosis in regions of dark apparent diffusion coefficient in 7 cases of high-grade glioma. Neuro Oncol. 2014;16(12):1599-1606. doi:10.1093/neuonc/nou142

[17] Chenevert TL, Malyarenko DI, Galbán CJ, et al. Comparison of Voxel-Wise and Histogram Analyses of Glioma ADC Maps for Prediction of Early Therapeutic Change. Tomogr (Ann Arbor, Mich). 2019;5(1):7-14. doi:10.18383/j.tom.2018.00049

[18] Lawrence LSP, Chan RW, Chen H, et al. Accuracy and precision of apparent diffusion coefficient measurements on a 1.5 T MR-Linac in central nervous system tumour patients. Radiother Oncol J Eur Soc Ther Radiol Oncol. 2021;164:155-162. doi:10.1016/j.radonc.2021.09.020

[19] Galla N, Chiang G, Chakraborty S, et al. Apparent diffusion coefficient changes predict survival after intra-arterial bevacizumab treatment in recurrent glioblastoma. Neuroradiology. 2017;59(5):499-505. doi:10.1007/s00234-017-1820-4

[20] Rathore S, Akbari H, Rozycki M, et al. Radiomic MRI signature reveals three distinct subtypes of glioblastoma with different clinical and molecular characteristics, offering prognostic value beyond IDH1. Sci Rep. 2018;8(1):5012-5087. doi:10.1038/s41598-018-22739-2

medRxiv preprint doi: https://doi.org/10.1101/2022.08.17.22278910; this version posted August 18, 2022. The copyright holder for this preprint (which was not certified by peer review) is the author/funder, who has granted medRxiv a license to display the preprint in perpetuity. It is made available under a CC-BY-NC-ND 4.0 International license .

[21] Kickingereder P, Neuberger U, Bonekamp D, et al. Radiomic subtyping improves disease stratification beyond key molecular, clinical, and standard imaging characteristics in patients with glioblastoma. Neuro Oncol. 2018;20(6):848-857. doi:10.1093/neuonc/nox188

[22] Gates EDH, Lin JS, Weinberg JS, et al. Guiding the first biopsy in glioma patients using estimated Ki-67 maps derived from MRI: conventional versus advanced imaging. Neuro Oncol. 2019;21(4):527-536. doi:10.1093/neuonc/noz004

[23] Bakas S, Reyes M, Battistella E, et al. Identifying the Best Machine Learning Algorithms for Brain Tumor Segmentation, Progression Assessment, and Overall Survival Prediction in the BRATS Challenge. Vol abs/1811.0.; 2018. http://arxiv.org/abs/1811.02629.

[24] Booth TC, Grzeda M, Chelliah A, et al. Imaging Biomarkers of Glioblastoma Treatment Response: A Systematic Review and Meta-Analysis of Recent Machine Learning Studies. Front Oncol. 2022;12:799662. doi:10.3389/fonc.2022.799662

[25] Bobholz SA, Lowman AK, Brehler M, et al. Radio-Pathomic Maps of Cell Density Identify Brain Tumor Invasion beyond Traditional MRI-Defined Margins. AJNR Am J Neuroradiol. 2022;43(5):682-688. doi:10.3174/ajnr.A7477

[26] Nguyen HS, Milbach N, Hurrell SL, et al. Progressing Bevacizumab-Induced Diffusion Restriction Is Associated with Coagulative Necrosis Surrounded by Viable Tumor and Decreased Overall Survival in Patients with Recurrent Glioblastoma. AJNR Am J Neuroradiol. 2016;37(12):2201-2208. doi:10.3174/ajnr.A4898

[27] Ruifrok AC, Johnston DA. Quantification of histochemical staining by color deconvolution. Anal Quant Cytol Histol. 2001;23(4):291-299.

[28] McGarry SD, Bukowy JD, Iczkowski KA, et al. Gleason Probability Maps: A Radiomics Tool for Mapping Prostate Cancer Likelihood in MRI Space. Tomogr (Ann Arbor, Mich). 2019;5(1):127-134. doi:10.18383/j.tom.2018.00033

[29] McGarry SD, Bukowy JD, Iczkowski KA, et al. Radio-pathomic mapping model generated using annotations from five pathologists reliably distinguishes high-grade prostate cancer. J Med Imaging. 2020;7(05):1-11. doi:10.1117/1.jmi.7.5.054501

[30] Clark K, Vendt B, Smith K, et al. The Cancer Imaging Archive (TCIA): Maintaining and Operating a Public Information Repository. J Digit Imaging. 2013;26(6):1045-1057. doi:10.1007/s10278-013-9622-7

[31] Scarpace L, Mikkelsen T, Cha S, et al. Radiology Data from The Cancer Genome Atlas Glioblastoma Multiforme [TCGA-GBM] collection. March 2016. https://wiki.cancerimagingarchive.net/x/sgAe.

[32] Chen L, Liu M, Bao J, et al. The correlation between apparent diffusion coefficient and tumor cellularity in patients: a meta-analysis. PLoS One. 2013;8(11):e79008. doi:10.1371/journal.pone.0079008

medRxiv preprint doi: https://doi.org/10.1101/2022.08.17.22278910; this version posted August 18, 2022. The copyright holder for this preprint (which was not certified by peer review) is the author/funder, who has granted medRxiv a license to display the preprint in perpetuity. It is made available under a CC-BY-NC-ND 4.0 International license .

[33] Akbari H, Rathore S, Bakas S, et al. Histopathology-validated machine learning radiographic biomarker for noninvasive discrimination between true progression and pseudoprogression in glioblastoma. Cancer. 2020;126(11):2625-2636. doi:10.1002/cncr.32790

[34] Liesche-Starnecker F, Prokop G, Yakushev I, et al. Visualizing cellularity and angiogenesis in newly-diagnosed glioblastoma with diffusion and perfusion MRI and FET-PET imaging. EJNMMI Res. 2021;11(1):72. doi:10.1186/s13550-021-00817-3

medRxiv preprint doi: https://doi.org/10.1101/2022.08.17.22278910; this version posted August 18, 2022. The copyright holder for this preprint (which was not certified by peer review) is the author/funder, who has granted medRxiv a license to display the preprint in perpetuity. It is made available under a CC-BY-NC-ND 4.0 International license .

7. Supplemental Material

Table 1: Demographic and clinical summary for included subjects)

	Train	Test
Number of Subjects	43	22
Age (years)	58.4 (14.1)	60.9 (11.7)
Overall Survival (months)	48.8 (71.2)	34.8 (42.3)
GBM/Non-GBM	29 / 14	18 / 4
Radiation treatment (y/n)	39 / 4	21 / 1
Chemotherapy (y/n)	39 / 4	20 / 2
Bevacizumab (y/n)	34 / 9	15 / 7
Tumor Treating Fields (y/n)	17 / 26	6 / 16

medRxiv preprint doi: https://doi.org/10.1101/2022.08.17.22278910; this version posted August 18, 2022. The copyright holder for this preprint (which was not certified by peer review) is the author/funder, who has granted medRxiv a license to display the preprint in perpetuity. It is made available under a CC-BY-NC-ND 4.0 International license .

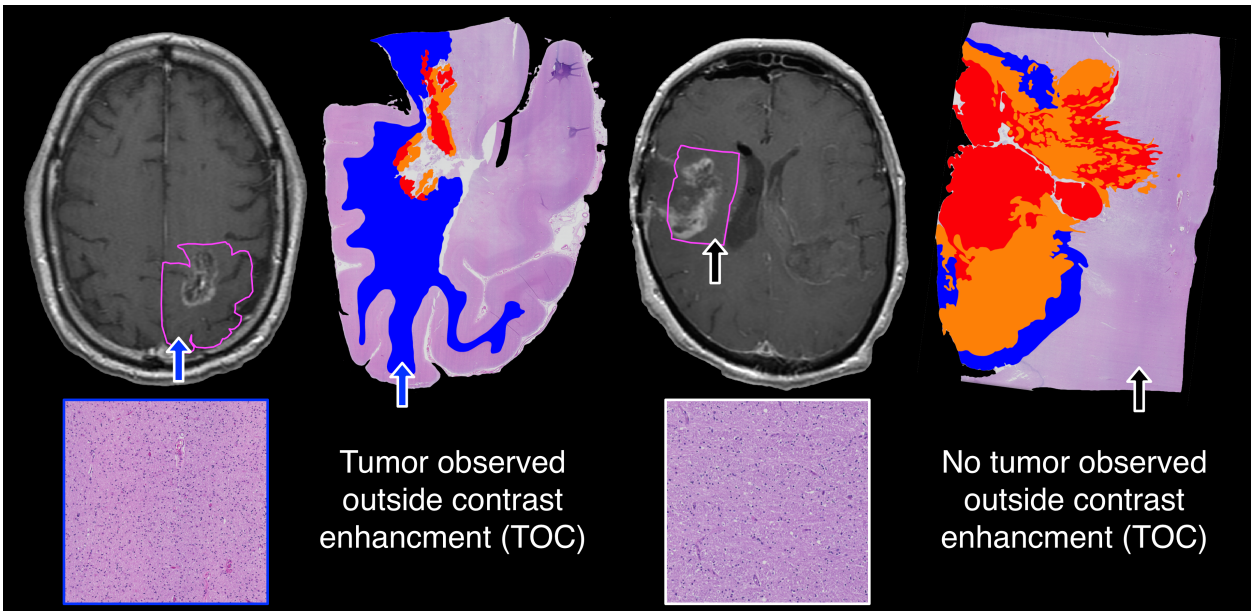

Supplemental Figure 1: Examples of patients with and without tumor outside of contrast

medRxiv preprint doi: https://doi.org/10.1101/2022.08.17.22278910; this version posted August 18, 2022. The copyright holder for this preprint (which was not certified by peer review) is the author/funder, who has granted medRxiv a license to display the preprint in perpetuity. It is made available under a CC-BY-NC-ND 4.0 International license .

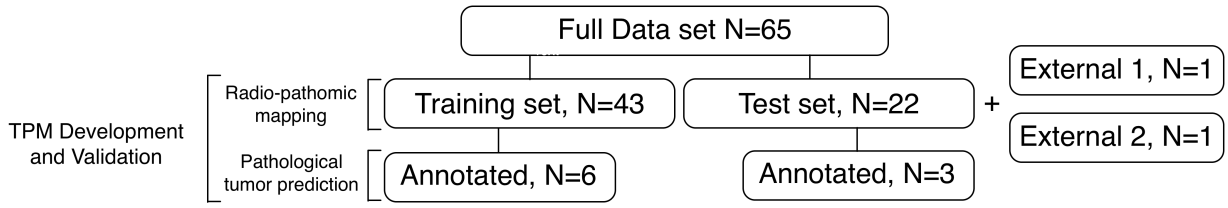

Supplemental Figure 2: Flowchart for the subjects included in each stage of the tumor probability map (TPM) model development